

# COHERENT FERROMAGNETIC PRECIPITATE AND ANOMALIES IN THE HEAT CONDUCTION AND THERMOPOWER OF $Mn_{2-x}Cr_xSb$ SINGLE CRYSTALS

A. KATTWINKEL, E. KRAUS, CH. KLEEBERG, T. GROŃ\*, AND K. BÄRNER

4. Phys. Institut der Universität Göttingen  
Bunsenstr. 13-15, 37073 Göttingen, Germany

(Received November 11, 1997; in final form March 17, 1998)

The heat diffusivity  $D$ , the electrical resistivity  $\rho$  and the thermoelectric power  $S$  of tetragonal  $Mn_{2-x}Cr_xSb$  single crystals with  $0.02 < x < 0.12$  have been measured in the temperature range of  $90 \text{ K} < T < 350 \text{ K}$  and along different crystal axes. The heat conductivity  $\kappa$  and  $\sigma = 1/\rho$  are anisotropic along the crystal axes  $a$ ,  $c$  with a ratio of 2:1.  $\kappa(T)$ ,  $\rho(T)$  and  $S(T)$  show anomalies at the spin reorientation temperature  $T_{Rm}$  of the matrix ( $M$ )  $Mn_{2-x}Cr_xSb$ , but also at that of the coherent ferromagnetic precipitate ( $P$ )  $Mn_{1.037}Cr_{0.11}Sb$ ,  $T_{Rp}$  which is assigned to variations in the spin dependent scattering at the  $M/P$  interfaces via changes in the relative orientation of the magnetization vectors of matrix and precipitate (spin valve effect).

PACS numbers: 75.30.Kz, 72.15.Eb, 72.15.Jf

## 1. Introduction

While  $Mn_2Sb$  is a metallic ferromagnet, chromium modified  $Mn_2Sb$ , i.e.  $Mn_{2-x}Cr_xSb$ , develops a first order antiferromagnetic ("afm")-ferri-magnetic ("fi") transition, which has been investigated in detail in former contributions [1-8]. A magnetic phase diagram which summarizes most of the previous works is given in Fig. 1. Recent claims that this material can be used as working material in magnetic cooling devices [9, 10] have stimulated interest in the thermal properties of these compounds. Specific heat capacity data were taken in the context of the afm-fi phase transition [9, 11] and yield an entropy change of 1-2 J/mol K, which is unusually high for a magnetic order-order transition. In contrast, heat

\*Institute of Physics, University of Silesia, Uniwersytecka 4, 40-007 Katowice, Poland.

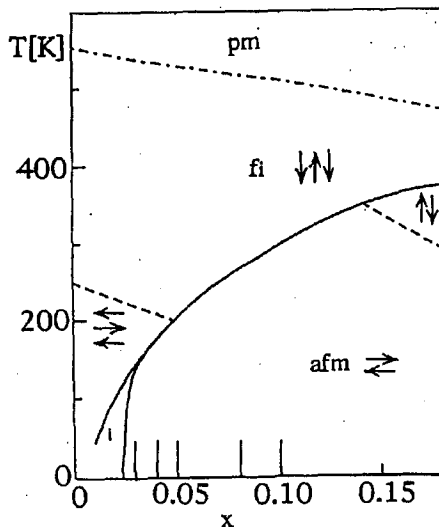


Fig. 1. Magnetic phase diagram  $T(x)$  of  $\text{Mn}_{2-x}\text{Cr}_x\text{Sb}$ . Vertical spin direction parallel to tetragonal axis. Nominal compositions of compounds used are marked of the  $x$ -axis (solid line — afm-fi order-order transition, dashed line — spin reorientation transition, dashed-pointed line — fi-pm order-disorder transition,  $i$  — intermediate spin state).

conductivity data are scarce and were so far only available for polycrystals [12]. However, the heat conductivity  $\kappa$  enters the figure of merit for working media as it determines the speed of the heat flow in and out of the volume and thus the cycle frequency.

In this contribution, we use the time resolved transient thermoelectric effect (“TTE”) for the determination of the heat diffusivity  $D$  and the thermoelectric power  $S$ . Although TTE allows a fast determination of  $D(T)$  and  $S(T)$  with no specific requirements on the sample size, it is recommended to verify and/or calibrate the results using established methods with at least one specimen. While in absolute value we can confirm earlier data, we find unexpected anomalies in the heat conductivity  $\kappa(T)$  and in  $S(T)$  which likely originate from a coherent planar precipitation of a very stable secondary ferromagnetic phase. According to our analysis these anomalies involve the internal surfaces matrix-precipitate ( $M/P$ ) and thus may be used for field-controlled and/or directed heat flow, if the surfaces are properly arranged.

## 2. Crystal preparation and experiments

### 2.1. Preparational

The single crystals of  $\text{Mn}_{2-x}\text{Cr}_x\text{Sb}$  (space group  $P^4/nmm$ ) were grown using the Bridgman-Stockbarger method as described in detail elsewhere [13]. Disks were cut (thickness  $\approx 0.5$  mm) from the regulus perpendicular to the growth direction using a diamond saw and were used to measure the magnetic anisotropy [9]; after that, rectangular (1 mm  $\times$  7 mm) strips were cut from the disks for the

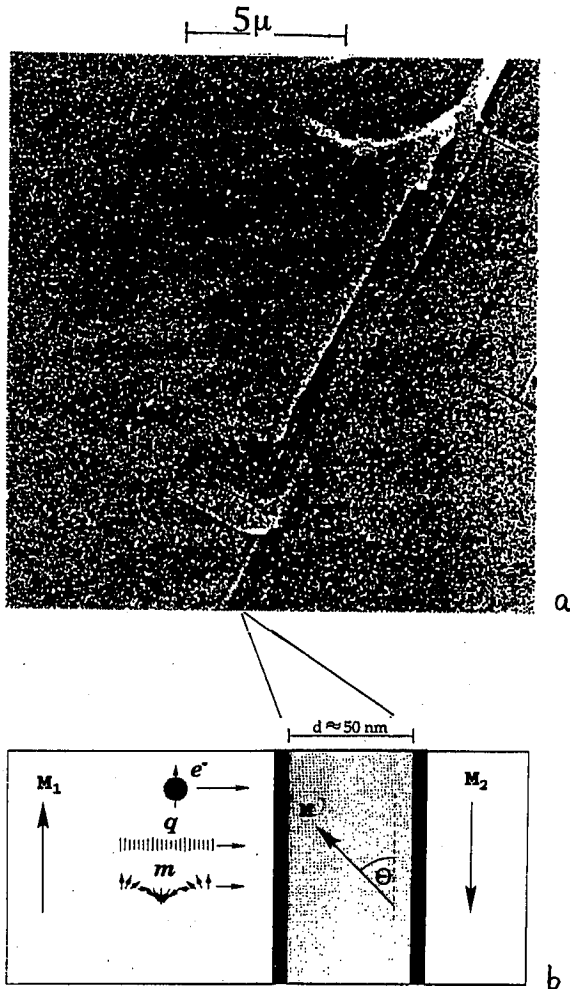


Fig. 2. Scanning electron micrograph of the (001)-plane of  $\text{Mn}_{1.96}\text{Cr}_{0.04}\text{Sb}$ , fine straight lines in (a) — coherent precipitate. (b) Sketch of planar ferromagnetic precipitate as a barrier for particles which contribute to the heat transport (electrons, phonons, magnons) and possible orientation of the internal polarizations.

measurement of the electrical conductivity, thermopower and heat diffusivity. In one case,  $x = 0.10$ , a strip of this size was prepared which was oriented parallel to the growth direction. Powder X-ray diffraction (Siemens 500) was done in order to insure a single phase; however, a small amount ( $< 3\%$ ) of a secondary phase,  $\text{Mn}_{1.07}\text{Cr}_{0.11}\text{Sb}$ , was identified; the composition was determined by the energy dispersive X-rays method (EDX, Cambridge). Using scanning electron microscopy (SEM), a coherent precipitation of this phase along the (101)-planes of  $\text{Mn}_{2-x}\text{Cr}_x\text{Sb}$  was observed (Fig. 2). A similar precipitation (0.5–3%) was observed earlier by Darnell et al. [14] and was tentatively identified as MnSb. It is found

that the precipitated phase,  $\text{Mn}_{1.07}\text{Cr}_{0.11}\text{Sb}$ , maintains its composition independent of  $x$ . The reguli were investigated in respect to homogeneity in Cr-content along the direction of growth and a maximal variation of 0.5% was calculated from the variation of the afm-fi transition temperature,  $T_S$ , except for the very end of the reguli which had to be sorted out. Inside a perpendicular cut slice the variation was much lower ( $< 0.1\%$ ), even down to the  $\mu\text{m}$  scale, according to EDX and SEM. Quantitative microanalysis made with the aid of EDX was also used to determine the final compositions and those were identical with the nominal compositions within  $< 10\%$ . Laue-diffraction was used to determine the crystallographic orientation of the samples. For that, projections of the isostructural  $\beta\text{-Sn}$  were used. (001)-planes of easy break made cuts along the tetragonal axis very difficult; therefore, most of the heat diffusivity measurements presented are in the tetragonal plane: however, small out of plane deviations of the long sample axis allowed us to estimate the  $a$ ,  $c$ -anisotropy.

## 2.2. Determination of the electrical and heat conductivities

The electrical conductivity is measured as usual using the four-point method; details are described in Ref. [9]. The transient thermoelectric effect "flash" method [15-18] measures the thermoelectric power  $S$  in arbitrary units and the thermal diffusivity  $D$ , which is proportional to the thermal conductivity  $\kappa$ , as  $D = \kappa/\rho_0 c_v$ . For the conversion of  $D$  into  $\kappa(T)$ ,  $c_v \approx c_p$  is taken from Refs. [9, 11] and  $\rho_0 = 7.04 \text{ g/cm}^3$  from Ref. [7].

Figure 3 shows the experimental setup used. In principle, a light pulse which is limited in space and time is focused on the one end of the sample, heats it up and a decaying thermovoltage is observed between the end faces of the sample. According to Sasaki and others [15, 16], the initial amplitude of this decay is proportional to the Seebeck effect, while the corresponding decay time is inversely proportional to the heat diffusion constant  $D$ .

For our experiment, the original arrangement is modified to increase the sensitivity at the expense of the time resolution, which must be only sufficient to observe the slow thermodiffusion. As a light source a halogen lamp (Osram, 500 W) was used. The beam was focused on the one end of the sample (illuminated section: 1 mm, sample length  $\approx 7$  mm). A mechanical shutter was positioned in between lamp and focusing lens in order to obtain a rectangular light pulse. Silver paint was used to make contact with the sample end faces and care was taken not to illuminate these contacts. The thermovoltage was then amplified by a factor of 100 (PMI OP 07, bandwidth 1 MHz), passed a passive 50 Hz filter and was then fed into an impedance transformer (Burr-Brown BUF 634, input impedance 8 M $\Omega$ , bandwidth 180 MHz) as the recording oscilloscope (Tektronix TEK DSO11402, bandwidth 500 MHz) has an input impedance of only 50  $\Omega$ . As the typical thermal relaxation times are  $> 1$  ms, we could switch to a 20 MHz bandwidth and thus increase the sensitivity of the input amplifiers (Tektronix 11A52). Figure 3 also shows one of the transients. For further data reduction, and after recording, the data were transmitted to a personal computer via an IEEE-interface. The sample holder was inserted into an optical cryostat, whose windows allowed for heating the sample with the light pulse while simultaneously detecting a fraction of it via

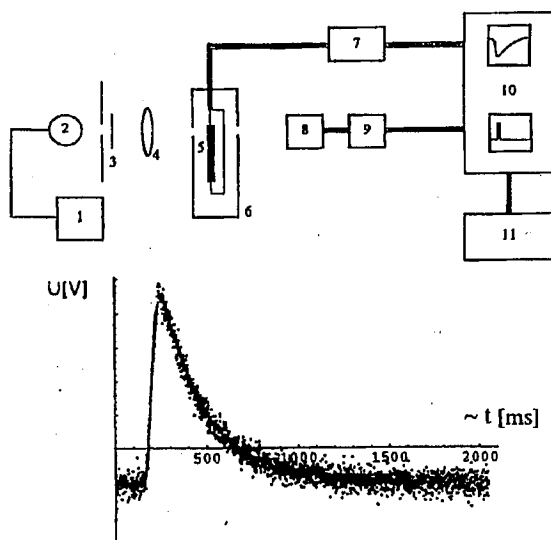


Fig. 3. Experimental set-up to measure the heat conductivity. Upper part — block diagram of the flash method: (1) power supply for lamp, (2) 500 W halogen lamp (Osram), (3) shutter, (4) lens, (5) sample, (6) sample holder, (7) amplifier, (8) PIN-diode, (9) impedance transformer, (10) oscilloscope, (11) PC for data acquisition. Lower part — typical thermovoltage transient  $U(t)$  and fit; one channel: 5 ms.

a photovoltaic cell for triggering purposes. The cryostat could be cooled down to 35 K using a helium compressor. Higher temperatures were obtained with an accuracy of  $\sim 1$  K using a regulated heater. From the observed thermovoltages and specific heat capacity data the local light induced increase in temperature was calculated to be less than 2 K. In the course of the data reduction, electrical offsets were subtracted, some Fourier-filtering and smoothing algorithms were used, which, however, were tested in respect to curvature deformation on known samples before application [19, 20]. After that, the transient  $V(t)$  is fitted to a solution of the heat diffusion equation

$$V(t) = S(T)[T(t, 0) - T(t, L)], \quad (1)$$

where

$$T(t, x) = \lim_{n \rightarrow \infty} (T_0/2) \int_0^{t_b} dt' \times \sum_{-n}^n \left\{ \operatorname{erf}((x+h-2nL)/\sqrt{4D}(t-t')) - \operatorname{erf}((x-h-2nL)/\sqrt{4D}(t-t')) \right\},$$

where  $\operatorname{erf}(x)$  is the error function,  $h$  — illuminated distance,  $D$  — thermal diffusion constant,  $L$  — sample length,  $t_b$  — duration of light pulse,  $S$  — thermoelectric

power, and  $T_0$  — the height of the rectangular initial temperature distribution. The summation in Eq. (1) converged and could usually be stopped at  $n = \pm 2$ , considering the accuracy of the raw data, which in turn allowed the absolute determination of  $D$  within about 5%.

Equation (1) does account for a finite sample length and a rectangular illuminated zone, but does require the sample thickness to be small against the sample length and the illumination time  $t_b$  small against the thermal diffusion time constant,  $L^2/4D$ . This condition was met by choosing appropriate light pulses and sample thicknesses  $\leq 0.5$  mm. Close to a zero crossing of  $S(T)$ ,  $D$  is difficult to determine because of very low signal to noise ratio of the TTE-amplitude. In these cases, sample independent,  $\leq 5\%$  low frequency undulations tend to appear in  $D(T)$ . These undulations are probably connected with an unintended correlation of successive transients: for example, if the temperature decay is very slow or if for the starting values of the  $(n + 1)$ th transient, the results of the  $n$ th transient are used. These artefacts, however, could be corrected making use of their systematics.

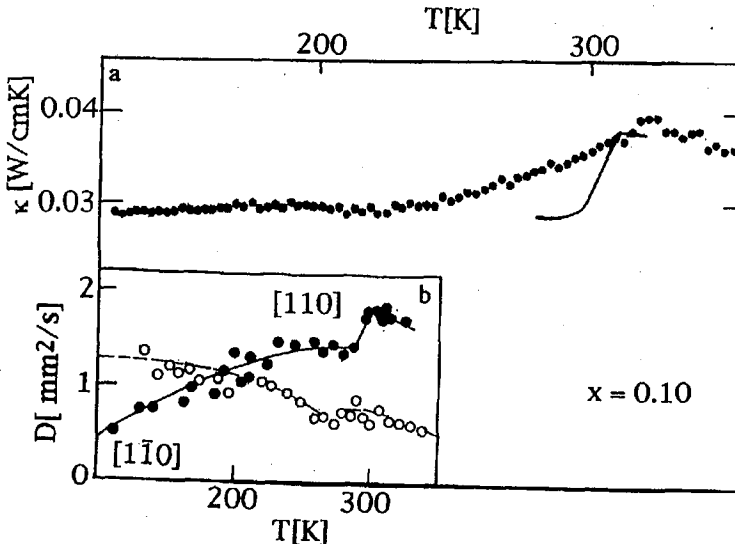


Fig. 4. Heat conductivity of  $\text{Mn}_{2-x}\text{Cr}_x\text{Sb}$ , (a)  $x = 0.1$ , measured conventionally along  $c$ , solid line —  $\kappa(T)$  on polycrystals according to Ref. [12]; (b) heat diffusivities in  $[110]$  (solid circles) and  $[1\bar{1}0]$  (open circles) directions versus temperature.

For the control experiment regarding  $\kappa(T)$  we used a differential method which is designed for long polycrystalline or single crystal rods (here always in growth direction) [19]. The sample holder was put in a flow cryostat and could be kept at a constant average temperature using a resistive heater. At one end of the sample another, smaller, resistive heater (SDM resistor,  $0.5 < P < 2$  W) provided a constant heating rate and with it a thermal gradient, which was measured using a differential thermocouple. Figure 4 shows  $\kappa(T)$  for  $x = 0.1$  measured classically and using the flash method, together with an earlier measurement on

a polycrystalline  $\text{MnAs}_{1.9}\text{Cr}_{0.1}\text{Sb}$  sample [12]. One observes an increase near the afm-fi transition at  $T_S = 315$  K in all cases, while the absolute values of  $\kappa$  are close. A shallow structure is observed close to 220 K. However, the phase diagram (Fig. 1) does not hold a corresponding transition. Although we used single crystals,

TABLE

Anomalies found in  $D$ ,  $\rho$ ,  $\kappa$ ,  $S$ ,  $c_p$  versus temperature. Indices  $D$ ,  $d$  [20]: from heat diffusivity measured by the flash method;  $s$ ,  $r$ ,  $k$ ,  $c$  from conventional  $S$ ,  $\rho$ ,  $\kappa$ ,  $c_p$  data.

$x$	$X1$	$T_{S1}$ (0-150 K)	$T_{S2}$ (0-200 K)	$X2$	$T_R$ (230-200 K)	$T'_R$ 240 K
0.02	105d			165d	229d	249d
0.03		103s	125s		220s	
0.04	101d		$T_{S1} = T_{S2}$ 187s 190r 187c	166d 160k 168D	210d 207k 204D	235D 243k 240d
0.05				163r 162d	$T_S = T_R$ (200-350 K) 220k 210s	238s 248d
0.06				163d	230d 233c 217s	
0.07					266s 272c 275d	252d $T_R \approx T'_R$
0.08				153d 165d	280k 270d	215k 220r 221d
0.09					273k 272s	210k
0.10					287s 315r 303d 323k 323c	198k 193k 196d
0.11	107d			163d	311s 319d	185d

the structures are broad which is likely due to the concentration gradients along the direction of growth. Thus, measurements on long single crystal rods will not show the fine structure and here is where the TTE-method, in using small sample slices preferably being cut perpendicular to the growth and concentration gradient, is superior. Nevertheless, characteristic temperatures which are connected with structures observed in the larger single crystal specimens using the classical method are summarized in Table together with those found using smaller single crystal pieces and the TTE-method.

### 2.3. Determination of the thermopower

According to Eq. (1), if the temperature increment is kept constant,  $V_0 \sim S(T)$ , i.e. the initial amplitude of the transient  $V_0$  measures the thermopower. However, there might be a shift between the measured voltages in both cases as  $V_0$

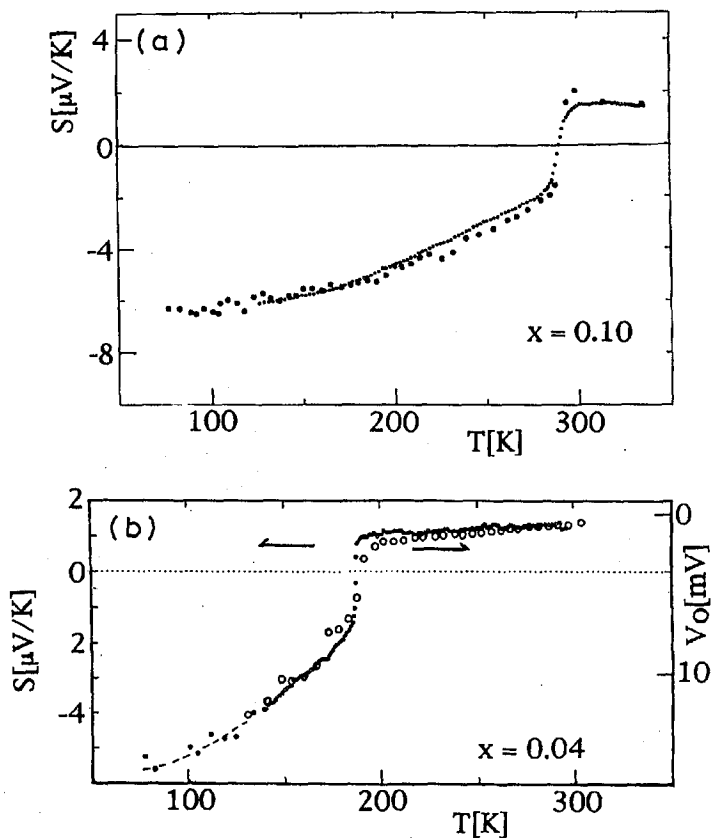


Fig. 5. Thermoelectric power versus temperature  $S(T)$  for  $x = 0.1$ , (a) using stationary (open circles) and quasi-stationary (solid circles) measuring modes,  $2^\circ$  off  $a$ -axis; (b) comparison of  $S(T)$  of  $x = 0.04$  as measured using the flash method (large circles) and the conventional methods (smaller circles),  $10.5^\circ$  off  $[-111]$ .

represents a thermochain: copper/silver-paint/sample/silver-paint/copper, while the conventional method measures the sample versus lead. For the control experiment regarding  $S(T)$  we used a standard setup [21] which was operated either in a stationary temperature mode or in a quasi-stationary mode where the average temperature is slowly increased while the temperature difference is kept constant via the temperature controller. The quasi-stationary mode has a better signal to noise ratio. Occasionally both modes were applied to the same sample in order to ensure consistency. As an example,  $S(T)$  of  $x = 0.1$  is shown in Fig. 5a. Figure 5b shows  $V_0(T)$  as compared to  $S(T)$  for  $x = 0.04$ . Allowing for a relative shift as indicated by the scales, both quantities are indeed proportional. Below the zero crossing of  $S$  there seem to be some irregularities. These might be connected with the precipitate or with concentration fluctuations which should have a large influence close to the bifurcation point of  $T_R$  and  $T_S$  (see Fig. 1).

### 3. Results

#### 3.1. Thermoelectric power

For  $x = 0.1$  in particular, one observes a sign change of  $S(T)$  at the combined afm $\rightarrow$ fi and spin reorientation temperature  $T_S = T_R = 290$  K (Fig. 5a). According to Fig. 1, for  $x > 0.045$ ,  $T_S$  and  $T_R$  coincide, while they are separate for  $x < 0.045$  (bifurcation point). Indeed, other than  $S(T)$  of  $x = 0.1$ ,  $S(T)$  of  $x = 0.03$  shows

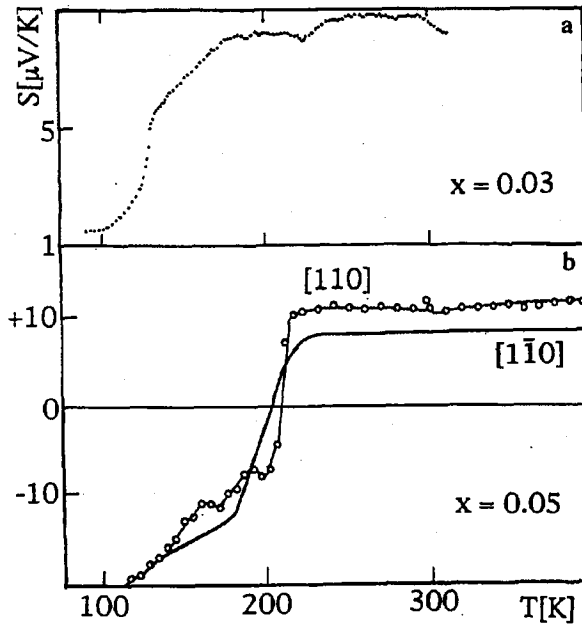


Fig. 6. (a)  $S(T)$  of  $x = 0.03$ , measured conventionally,  $12^\circ$  off  $a$ -axis; (b)  $S(T)$  of  $x = 0.05$  along  $[110]$  and  $[1\bar{1}0]$  direction.

two anomalies, a step at  $T_S = 125$  K and a minimum or change of slope at  $T_R = 225$  K (Fig. 6a). In fact, for  $x = 0.03$ , the second bifurcation point, which introduces the intermediate (*i*) magnetic phase, should have just passed. This would explain that the increase in  $S(T)$  around 125 K apparently occurs in two steps.

In one case, i.e.  $x = 0.05$ , we have measured  $S(T)$  conventionally, but for two different crystal directions (Fig. 6b). We observe only a small difference in  $S$  between the two in tetragonal plane orientations, as expected. As with  $x = 0.04$ , irregularities are observed below the zero crossing.

### 3.2. Electrical conductivity

Our resistivity versus temperature curves  $\rho(T)$  are consistent with earlier data where only one crystal direction (in the tetragonal plane) was measured [22]. We observe a small difference in the phase transition temperature and the width of the transition for the samples oriented along  $a$ ,  $c$  which is probably due to a different gradient in Cr-content. We find a factor of 2 between the resistivities along  $c$ ,  $\rho_{\parallel}$ , and along  $a$ ,  $\rho_{\perp}$ , in the afm phase while they differ only by a factor of 1.3 in the fi phase (Fig. 7). The inset shows  $\rho(T)$  of  $x = 0.08$  in  $a$ -direction for

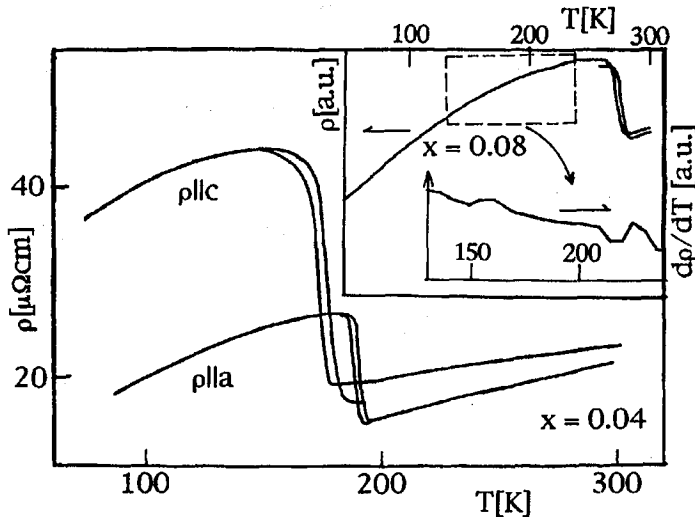


Fig. 7. Anisotropy of the resistivity  $\rho$  for  $x = 0.04$ , upper/lower curve — measurement along  $a$ ,  $c$ ; inset —  $\rho$  and  $d\rho/dT$  of  $x = 0.08$  versus  $T$  along  $a$ .

$x = 0.08$ . Although  $T_R = T_S$  in this case, the derivative  $d\rho/dT$  reveals an anomaly close to 225 K and eventually one at 150 K, both of which cannot be assigned to phase transitions of the matrix and therefore are tentatively attributed to the precipitate.

### 3.3. Heat diffusivity

Figure 8 shows  $D(T)$  of a  $x = 0.04$  sample with a long axis in  $[-111]$ -direction. The diffusivity slowly decreases and is fairly reproducible. However, apparently the

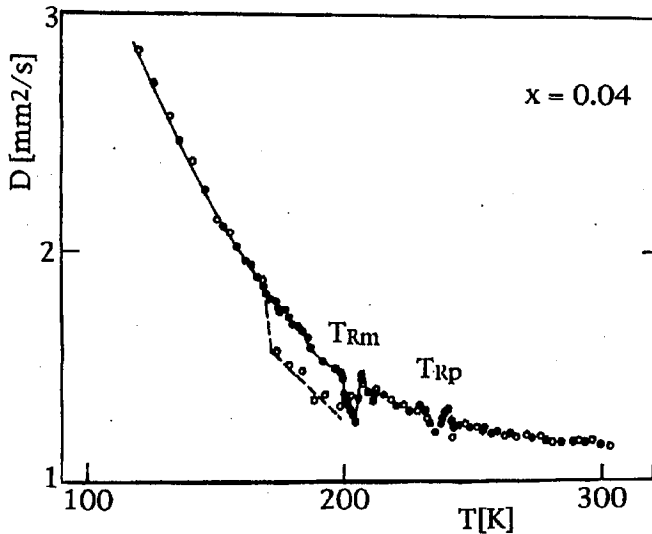


Fig. 8. Heat diffusivity versus temperature  $D(T)$  of  $\text{MnAs}_{1.96}\text{Cr}_{0.04}$   $10.5^\circ$  off  $[-111]$ ; two consecutive runs are marked by open circles.  $T_{Rp}$ ,  $T_{Rm}$  characteristic temperatures.

return to the afm phase or its spin-reorientation is delayed in the second run which might be due to strains which are introduced when the first passing through the transition occurs. Anomalies are observed at  $T_{Rm}$  and  $T_{Rp}$ , these temperatures coincide indeed with the reorientation temperatures of the matrix  $T_{Rm}$  (see Fig. 1) and of the precipitate  $T_{Rp}$  (see below). Similar anomalies in  $D$  are also found with other samples and in other temperature regimes (see Table). The anomalies are observed independent of crystal direction, but always differ somewhat in magnitude, suggesting extrinsic causes.

In the case of  $x = 0.10$  measurements of  $D$  were taken in two in tetragonal plane directions (the inset of Fig. 4). One finds a twofold anisotropy, which is inverted at 200 K. This is not consistent with an intrinsic anisotropy, as this should be zero (isotropic) or fourfold in the tetragonal plane. Darnell et al. [14] have made a similar observation, i.e. he found a twofold symmetry in torque measurements, which he attributed to a coherent precipitation of a highly anisotropic secondary magnetic phase, i.e.  $\text{MnSb}$ . In our samples,  $\text{Mn}_{1.07}\text{Cr}_{0.11}\text{Sb}$  is the precipitate; it influences the magnetocrystalline anisotropy of the matrix [9] and apparently also the heat conductivity.

#### 3.4. Magnetocrystalline anisotropy of the precipitated phase

As the mononictide  $\text{MnSb}$ , which is similar to our precipitated phase, has a spin reorientation not far from the second anomaly, i.e. at 270 K [23], it was suggested that the extra anomalies are connected with the spin reorientation temperature of the precipitate. Thus we have prepared a large single crystal of  $\text{Mn}_{1.07}\text{Cr}_{0.11}\text{Sb}$  and have measured its magnetocrystalline anisotropy. The mononictide is a stronger ferromagnet ( $\mu_0 = 3.8\mu_B/\text{Mn}$ ) as  $\text{Mn}_2\text{Sb}$  ( $\mu_0 = 1\mu_B/\text{Mn}$ ),

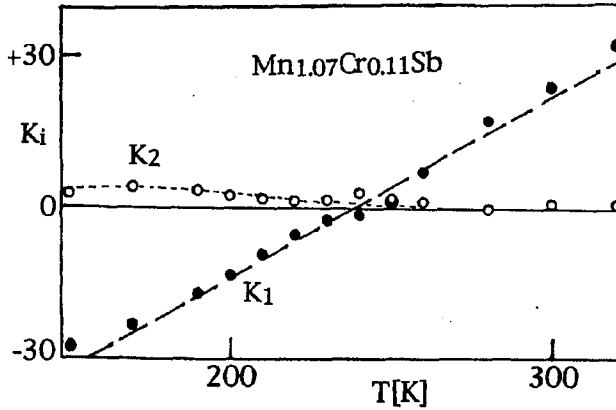


Fig. 9. Anisotropy constants  $K_1$ ,  $K_2$  in [ $10^3 \text{ Jcm}^{-3}$ ] of the free precipitated phase  $\text{Mn}_{1.07}\text{Cr}_{0.11}\text{Sb}$  versus temperature.

has a hexagonal lattice ( $a = 4.208 \text{ \AA}$ ,  $c = 5.702 \text{ \AA}$ ), a Curie temperature  $T_C = 365 \text{ K}$  and indeed shows a spin reorientation at  $T_{\text{Rp}} = 240 \text{ K}$  (Fig. 9). Details of the apparatus and data reduction (Sucksmith-) procedure are given in Refs. [9, 23, 24].  $T_{\text{Rp}}$  is close to a whole set of anomalies, see Table. Because of lattice mismatch, the planar precipitate is probably under stress. Therefore, depending on the stress situation in each sample, the actual spin reorientation in the precipitate might be shifted somewhat against that of the free crystal. However, as the precipitate contributes only  $< 5 \text{ vol\%}$  while its physical parameters  $\rho$ ,  $\kappa$ ,  $S$  are close to that of the matrix [23, 25–28], the extra anomalies should not be detectable at all. As we find them in the same order of magnitude as the matrix related ones, any explanation in terms of a precipitate volume effect or a combined matrix/precipitate current path effect would meet difficulties. On the other hand, the observed deposition of the precipitate volume fraction in 50 nm sheets which completely surround the matrix domains (Fig. 2) suggests an effect which involves the large area provided by the internal surfaces.

#### 4. Discussion

##### 4.1. Intrinsic anisotropy of the conductivity and the heat conductivity

We observe differences up to a factor of 2 between the matrix conductivities along  $c$  and along  $a$ . The specific structure of  $\rho(T)$  and the step have been connected with different magnon or magnon–phonon mixed mode scattering in the two magnetic phases [26] and/or an electron band reconfiguration which occurs together with the afm/fi coupled phase transition [29]. For tetragonal symmetry (space group  $P^4/nmm$ ) and transformation to the crystal axes the heat conductivity tensor should read [27]

$$\kappa = \begin{pmatrix} \kappa_{\perp} & 0 & 0 \\ 0 & \kappa_{\perp} & 0 \\ 0 & 0 & \kappa_{\parallel} \end{pmatrix} . \quad (2)$$

The same should hold for the heat diffusivity tensor  $D_{ij} = \kappa_{ij}/\rho_0 c_v$  and the conductivity tensor  $\sigma_{ij}$ . From slightly out of tetragonal plane measurements we deduce a ratio of 1.75:1 for the heat diffusivities along  $a$  and  $c$  for  $T \leq T_S$  [20]. As this is close to the ratio of the conductivities, one is tempted to ask for the Lorenz number  $L = \kappa/\sigma T$  of these compounds. For  $x = 0.1$ , close to the afm-fi transition,  $T_S$ ,  $L(T)$  crosses  $L_0$  and then stays close for  $T > T_S$  ( $0.9L_0$ ), suggesting a stronger contribution of the electron gas to the heat conduction in the ferrimagnetic phase, which has indeed the higher electrical conductivity. For  $T < T_S$ , however,  $L(T)$  deviates up to  $4L_0$ . As one usually writes [30]

$$\kappa = \kappa_{el} + \kappa_{ph} + \kappa_m, \quad \sigma = \sigma_{el} \quad (3)$$

and as there is rarely a large step of  $\kappa$  at  $T_S$ , but one of  $\sigma$ , at the afm-fi transition the changes in the three terms of Eq. (3) always almost balance. Then again, the observation of extra structure inside of a magnetic phase, say  $\Delta\kappa$ , strongly suggests extrinsic causes.

Except for the anomalies, the temperature dependence of the heat conductivity follows expectation, i.e. it should drop like  $T^{-2}$  [31] with a tendency for saturation at high temperatures [32]. The afm-fi transition can be detected, but here only through a dip close to  $T_S$ , i.e. for  $x = 0.04$ ,  $\kappa$  is almost exactly equal in both phases. The second anomaly is close to 240 K and therefore probably related to the precipitate.

#### 4.2. Thermoelectric power

For  $x > 0.04$ , the thermoelectric power goes through a zero crossing at  $T_S$ . This suggests two types of carriers  $n$ ,  $p$ , a two band model and consequently  $S$  should be a composite [33, 20]

$$S = S_n(\sigma_n/\sigma) + S_p(\sigma_p/\sigma) = (S_n n b + S_p p)/(n b + p) \quad (4a)$$

( $b = \mu_n/\mu_p$ : mobility ratio). This is supported by the low value of the Hall constant given by [22] for both the afm and fi phases,  $R_H \approx 3 \times 10^{-12}$  V cm/GA. This would give a carrier concentration of about  $2 \times 10^{22}$  cm $^{-3}$ , while for transition metal compounds of this type usually  $10^{21}$  cm $^{-3}$  are reported [21]. According to Eq. (4a) the zero crossing in  $S(T)$  does not necessarily coincide with the transition if one assumes that at  $T_S$  the mobility ratio changes but not  $n$ ,  $p$  [22].  $T_S$  as determined from  $S(T)$  is indeed usually lower as  $T_S$  determined from the specific heat capacity  $c_p(T)$  (see Table). Because of the two-band character of  $\text{Mn}_{2-x}\text{Cr}_x\text{Sb}$  a shift might be found also for  $\rho$ ,  $\kappa$ .

As we have a magnetic semimetal, both the partial conductivities  $\sigma_n$ ,  $\sigma_p$  and the partial thermopowers  $S_n$ ,  $S_p$  should contain a magnetic and an electronic contribution

$$S^i = S_e^i + S_m^i, \quad i = n, p. \quad (4b)$$

$S_e$  is practically the diffusion thermopower, which is linear in  $T$  but might show saturation tendencies at high temperatures [33]. Phonon and magnon drag effects could occur but are supposed to be negligible in the temperature range considered here. The main contribution should come from the coupling to excitations of the spin system. Kasuya [34] has calculated the magnon contribution to  $S$ , and has

found a broad maximum for  $0 < T < T_C$ , with  $S_m$  disappearing at  $T = 0$  and  $T = T_C$ . The broad structures and the shallow maxima (minima) observed in  $S(T)$  indeed point to a dominant magnon contribution. Then, a small linear contribution from isotropic magnetic scattering is always superimposed, but would be difficult to separate from the diffusion thermopower.

For  $x > 0.4$ , apparently the partial properties of the electrons dominate, while for  $T > T_S$  those of the holes. Alternatively, changes in the electronic structure through the introduction of a new magnetic Brillouin zone (BZ) [35, 36] could occur, in particular introducing hole-like carriers on the one side of the transition and electron-like carriers on the other. However, for the ferrimagnetic–antiferromagnetic transition observed in  $Mn_{2-x}Cr_xSb$ , the BZ changes should not be very large as antiferromagnetism constitutes a special case of ferrimagnetism and as metallic conduction persists through the transition. Also, it is generally acknowledged that the Sb  $2p$ -states overlap with the Mn(Cr)  $3d$ -states, introducing a semimetallic condition with two kinds of carriers ( $2p$ -holes and  $3d$ -electrons). Moreover, the systematic downward shift of the zero crossing of  $S(T)$  (Table) would be hard to explain, as it should occur at  $T_S$  if initiated by a BZ change. Therefore we propose to stay with a two-band situation, while BZ changes would allow us to discontinuously change the two carrier transport parameters on both sides in narrow range.

#### 4.3. Spin-valve effect

We submit that the non-matrix related anomalies are somehow connected with the precipitate. Consistently, only the transport properties but not the volume properties  $M(T)$  and  $c_p(T)$  show these extra structures [9]. Thus, the magnetic state does not change there. The fact that anomalies occur at both reorientation transitions (matrix or precipitate) points to a relation with the relative orientation of the magnetic polarization in the two phases. This relative orientation should indeed change with the temperature. If, for example, the anisotropy constants  $K_i$  go to zero at  $T_{Rp}$ , demagnetization forces  $M_p$  parallel to the plane, while with  $K_i > 0$ ,  $M_p$  would tend to lie in the easy direction of the precipitate. During this change the matrix magnetic polarization would be constant. While we can conclude a change in relative polarization on both sides of the interface with the temperature, the exact nature of the  $M/P$ -interface is still somewhat unclear. From the SEM-contrast we conclude that the lattice mismatch is probably reduced through dislocations. Moreover, since impurities or other secondary phases often accumulate at such interfaces, it might be that we have a nonmagnetic or even insulating surface layer (Fig. 2b). In such situations, spin dependent scattering which depends on the relative orientation of the magnetization in the adjoining regions occurs at the boundaries. For example, the conductance  $G$  of a ferromagnetic metal – paramagnetic insulator – ferromagnetic metal (FM–PI–FM) structure, has been calculated to be (spin-valve effect [37])

$$G = G_0(1 + P^2 \cos \theta); \quad \theta \angle M_1, M_2 : P \leq 1 \text{ polarization factor.} \quad (5)$$

The angular function originates from the spinor transformation which is involved in the tunneling calculation. In other cases, i.e. for a ferromagnetic metal – para-

magnetic metal – ferromagnetic metal (FM–PM–FM) structure, one has calculated a dependence on  $\sin \theta$  [38], suggesting that a combination of both functions is also possible.

Accordingly, we have calculated the temperature dependence of the angle between the matrix magnetization  $M_m$  and the magnetization of the precipitate  $M_p$ ,  $\theta(T)$ , for two situations, one assuming no strains and the easy direction of the precipitate out of plane, the other assumes the easy direction in plane but with in plane strains in the precipitate.

*Case 1: Out of plane easy direction in the precipitate*

Assuming the magnetocrystalline energy density of the precipitate to be  $E_a = K_0 + K_1 \sin^2 \Phi + \dots$ , together with a shape anisotropy  $E_f = (1/2)M_s^2 N \sin^2 \theta$ , the total energy is  $E_g = E_f + E_a$ . Here, specifically,  $\Phi = 45^\circ - \theta$  and  $K_1 = \alpha(T - T_R)$  (Fig. 10a). From the equilibrium condition  $\partial E_g / \partial \theta = 0$  one then arrives at  $\theta(T)$

$$T - T_R = (M_s^2 N / 2\alpha) \tan(2\theta). \tag{6a}$$

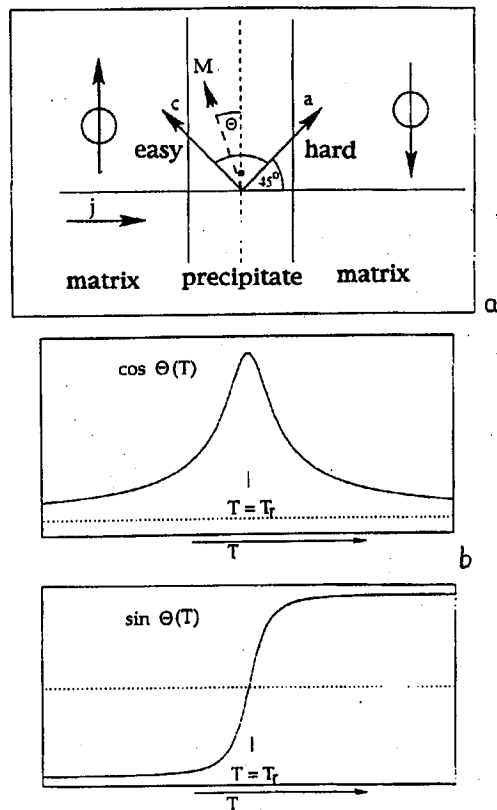


Fig. 10. (a) Change of magnetic polarization close to the reorientation temperature  $T_R$  of the precipitate due to competition of shape and magnetocrystalline anisotropies. (b)  $\cos \theta(T)$ - and  $\sin \theta(T)$ -type of anomaly,  $\theta \perp M_1, M_2$  (for more details see the text).

Figure 10b now shows  $\cos \theta(T)$  and  $\sin \theta(T)$ , which single or in combination should be proportional to some of the observed transport anomalies.

#### Case 2: Internal strains

In this case, one easy direction of the precipitate is parallel to the plane ( $\theta = 0$ ) and the strains are represented by an effective field  $H_\sigma$ , which is also in plane. The corresponding (Zeeman-type) energy is  $-H_\sigma M_s \cos \theta$ . Adding a magnetocrystalline energy as given above and applying the equilibrium condition, it yields now

$$T - T_R = (-H_\sigma M_s / 2\alpha)(1 / \cos \theta). \quad (6b)$$

As  $|1 / \cos \theta|$  cannot be smaller than 1, there are no solutions for  $T_R < T < T_R - H_\sigma M_s / 2\alpha = T'_R$ . This means, that the onset of the anomaly is shifted to  $T'_R$ . A similar shift we obtain in this configuration if we consider only the shape anisotropy:  $T'_R = T_R - M_s^2 N / 2\alpha$ . If the demagnetization is involved, we expect the location of the precipitate related anomalies to be shifted when the matrix changes from the afm to the fi (lower demagnetization) state. This is indeed observed for the anomaly designated as  $T'_R$  in Table: while in the fi matrix state ( $x < 0.07$ ) the values are close to 240 K, they are generally lower (ca. 200 K) in the afm state of the matrix. Considering the interface paramagnetic, we may take over the valve-effect calculation given above to our ferrimagnetic metal - paramagnetic metal - ferromagnetic metal (FiM-PM-FM) interface. So far we have not found any equivalent calculation for an antiferromagnetic metal - paramagnetic metal - ferromagnetic metal (AFM-PM-FM) structure. However, from the very nature (spin dependent tunneling) of those calculations we can expect a dependence on the angle between the sublattice magnetizations, here too.

Stress related shifts only depend on  $H_s$  and  $M_s$  both of which can be considered approximately constant for  $T < 240$  K. Thus, the anomalies found at lower temperatures, designated X1, X2, which are virtually independent of  $x$  and of the matrix state, might be explained that way. Note that this interpretation only requires a delayed change of the spin orientation close to the interface (interface spin clamping), this could happen even if in the volume spin state and orientation have changed already.

#### Acknowledgments

The authors thank the Deutsche Forschungsgemeinschaft (DFG) and the German Academic Exchange (DAAD) for continuous support, E. Gmelin, R. Plischke and U. Sondermann for some of the measurements and J. Warczewski for helpful discussions.

#### References

- [1] W.H. Cloud, H.S. Jarrett, A.E. Austin, E. Adelson, *Phys. Rev.* **120**, 1969 (1960).
- [2] W.H. Cloud, T.A. Bither, T.J. Swoboda, *J. Appl. Phys.* **32**, 55S (1961).
- [3] A.E. Austin, E. Adelson, W.H. Cloud, *Phys. Rev.* **131**, 1511 (1963).
- [4] H.S. Jarrett, *Phys. Rev. A* **134**, 942 (1964).
- [5] W.A. Doerner, R.B. Flippen, *Phys. Rev. A* **137**, 926 (1965).

- [6] T. Kanomata, T. Kawashima, T. Kaneko, H. Takahashi, N. Mori, *Jpn. J. Appl. Phys.* **30**, 541 (1991).
- [7] T.J. Swoboda, W.H. Cloud, T.A. Bither, M.S. Sadler, H.S. Jarrett, *Phys. Rev. Lett.* **4**, 509 (1960).
- [8] Ch. Kleeberg, E. Kraus, K. Bärner, T. Groñ, U. Sonderman, *Radiat. Eff. Defects Solids* **143**, 1 (1997).
- [9] Ch. Kleeberg, Ph.D. Thesis, Göttingen 1995.
- [10] N.V. Baranov, P.E. Markin, Y.A. Chrulev, *Pis'ma Journ. Techn. Phys.* **18**, 20 (1992).
- [11] R.B. Flippen, F.J. Darnell, *J. Appl. Phys.* **34**, 1094 (1963).
- [12] K. Sato, M. Nakazima, T. Miyazaki, Y. Isikawa, K. Mori, *J. Appl. Phys.* **55**, 2036 (1984).
- [13] H.J. Kohnke, Diploma Thesis, Göttingen 1991.
- [14] F.J. Darnell, W.H. Cloud, H.S. Jarrett, *Phys. Rev.* **13**, 647 (1963).
- [15] M. Sasaki, H. Negeshi, M. Inoue, *J. Appl. Phys.* **59**, 796 (1986).
- [16] M. Kobayashi, H. Satoh, N. Kamegashire, K. Inoue, *J. Alloys Comp.* **192**, 93 (1993).
- [17] J.W. Schünemann, H.J. Kohnke, K. Bärner, *J. Magn. Magn. Mater.* **82**, 204 (1989).
- [18] J. Liebe, Diploma Thesis, Göttingen 1995.
- [19] F.X. Eder, *Moderne Messmethoden der Physik, Teil II, Thermodynamik*, VEB Deutscher Verlag der Wissenschaften, Berlin 1972, p. 320.
- [20] E. Kraus, Diploma Thesis, Göttingen 1995.
- [21] U. Neitzel, K. Bärner, *J. Phys. C, Solid State Phys.* **11**, 4975 (1978).
- [22] P.E. Bierstedt, *Phys. Rev.* **132**, 669 (1963).
- [23] H.J. Kohnke, V. Dankelmann, Ch. Kleeberg, J.W. Schünemann, K. Bärner, A. Vetcher, G.A. Govor, *Phys. Status Solidi B* **191**, 511 (1995).
- [24] A. Kattwinkel, Diploma Thesis, Göttingen 1997.
- [25] Ch. Kleeberg, A. Vetcher, H. Dunkel, J.W. Schünemann, K. Bärner, *J. Alloys Comp.* **262-263**, 502 (1997).
- [26] V. Dankelmann, H.J. Kohnke, J.W. Schünemann, K. Bärner, S. Buzhinsky, I.V. Medvedeva, *J. Alloys Comp.* **209**, 305 (1994).
- [27] H. Berg, *Phys. Status Solidi A* **40**, 559 (1977).
- [28] H.J. Kohnke, Ch. Kleeberg, V. Dankelmann, K. Bärner, J.W. Schünemann, *J. Alloys Comp.* **239**, 150 (1996).
- [29] H.S. Jarrett, P.E. Bierstedt, F.J. Darnell, M. Sparks, *J. Appl. Phys.* **32**, 57S (1961).
- [30] H.W. Gronert, D.M. Herlach, E.F. Wassermann, *Europhys. Lett.* **6**, 641 (1988).
- [31] J.M. Ziman, *Prinzipien der Festkörpertheorie*, Harri Deutsch, Frankfurt 1975, p. 233.
- [32] K.H. Hellwege, *Einführung in die Festkörperphysik*, Springer, New York 1988.
- [33] N.F. Mott, H. Jones, *The Theory of the Properties of Metal and Alloys*, Clarendon, Oxford 1936.
- [34] T. Kasuya, *Progr. Theor. Phys.* **22**, 227 (1959).

- [35] M.M. Amado, R.P. Pinto, M.E. Braga, M.S. Rogalski, J.B. Sousa, *J. Appl. Phys.* **81**, 5784 (1997).
- [36] K. Durczewski, M. Ausloos, *Phys. Rev. B* **53**, 1762 (1996).
- [37] J.C. Slonczewski, *J. Phys. (France) C* **8**, 1629 (1988).
- [38] L. Berger, *IEEE Trans. Magn.* **31**, 3871 (1995).